INTERNATIONAL JOURNAL FOR NUMERICAL METHODS IN FLUIDS
Int. J. Numer. Meth. Fluids 2009; **61**:810–826
Published online 23 February 2009 in Wiley InterScience (www.interscience.wiley.com). DOI: 10.1002/fld.1953

Development and evaluation of a model for soil–air fluidized bed rheological behavior

David M. Fox[1] and Joon Sang Lee[2, 3, *, †]

[1]*U.S. Army RDECOM-TARDEC, AMSRD-TAR-R/MS 211, Warren, MI, U.S.A.*
[2]*Department of Mechanical Engineering, Wayne State University, 5050 Anthony Wayne Dr. #2100, Detroit, MI 48202, U.S.A.*
[3]*Department of Mechanical Engineering, Yonsei University, Seoul, Korea*

SUMMARY

The ground vehicle mine blast mitigation problem represents a research topic that has recently been generating a very high level of interest and activity. Many aspects of the physics of the problem have been extensively researched. One area that has been neglected, however, is that aspect of the blast threat that relates to the rheology and flow, subsequent to ignition of the explosive, of the relatively energetic mixture of air and soil, sometimes referred to as ejecta.

Methods developed for the study of fluidized beds that are used in, e.g. the chemical and power generation process industries, were adapted in order to more clearly define the rheology of air–glass bead mixtures and also of air–soil mixtures that comprise the ejecta. Continuity and momentum balance equations developed for fluidized beds were adapted, using physical properties of glass beads and soils, into a form relates to the properties of mine blast ejecta.

These equations were then discretized and solved, for a relatively simple geometry, in order to validate the model and gain a general sense of the flow behavior of particle–air blends. Parametric studies were performed to estimate the variation of the rheology of the air–particle mixtures as a function of the particle diameter and the sphericity of the particles. Finally, the flow properties of a couple of real soils were investigated via application of the two-phase flow model. Copyright © 2009 John Wiley & Sons, Ltd.

Received 25 March 2008; Revised 22 September 2008; Accepted 24 September 2008

KEY WORDS: air–soil; rheology; blast; flow; particle properties; multi-component; ejecta; fluidized bed; CFD; mine blast; multi-phase

INTRODUCTION

As a result of recent world events, the ground vehicle mine blast mitigation problem constitutes a research topic that has been generating increased interest and activity. Physical tests of vehicle

*Correspondence to: Joon Sang Lee, Department of Mechanical Engineering, Wayne State University, 5050 Anthony Wayne Dr. #2100, Detroit, MI 48202, U.S.A.
†E-mail: joonlee@wayne.edu, cfdguy2003@hotmail.com

systems that are subjected to blast loads are relatively expensive. The judicious development and use of properly conceived computational and analytical methods can be used to significantly reduce the scale and cost of experimentation and thus moderate the cost of development of mine-protected vehicles.

Analysis of the mine blast problem typically involves evaluation of the dynamic behavior and interaction of high explosives, soil, air and structures such as the armored plates associated with commercial and military ground vehicles. The blast load from air and gaseous high explosive reaction products is typically modeled by using either reduced-order techniques based on pre-processed data [1] or as a mixture of gaseous fluids using an arbitrary Lagrange–Euler treatment [2].

The Mohr–Coulomb model constitutive treatment of the viscoplastic properties of the soil in its relatively dense and granular form [3, 4] equates the deviatoric components of stress in the solid–soil mass to a function of soil cohesion strength, angle of friction, and hydrostatic pressure and has reached a fairly advanced state of evolution. In fact more recent work includes the development and validation of an improved viscoplastic cap model that includes strain rate effects [5] and has been shown to be suitable for modeling of time-dependent problems such as that of mine blast.

The Mohr–Coulomb approach represents a suitable technique for the part of the problem that involves soil compaction and crater forming, but soil in the somewhat more dilute concentration levels that are observed in blast ejecta has been modeled most frequently either by means of techniques such as smoothed particle hydrodynamics, or by means of the multi-material arbitrary Lagrange–Euler method, apparently, in the case of the latter, with the tacit assumption of Newtonian rheology for the soil component of the mixture, e.g. Laine *et al.* [6], and Neuberger *et al.* [4]. It does not seem entirely clear whether the arbitrary Lagrange–Euler modeling methods currently used for soil ejecta, i.e. soil ejected at a high velocity away from the sources of explosions, yield sufficiently accurate rheological predictions.

Bergeron *et al.* [7] and Hlady [8] have reported, based on measurements from physical tests, that soil ejecta tends to have a significant mechanical loading effect on panels. Depending on the depth of burial of the mine and the type and condition of the soil, the soil ejecta could actually present the most significant loading effect on the surfaces of the vehicles. A more properly conceived and implemented constitutive model for the rheology of the multi-phase behavior of the air–soil mixture would be expected to allow improved understanding of this portion of the physics of blast and to, by means of the concomitant improved fidelity of numerical models, enable better designs for mine-protected vehicles.

Multi-phase flow has been investigated and analyzed for the treatment of problems with flow regimes that exhibit some similarities to the mine blast soil–air mixture. These analyses were performed for application in fields as diverse as coal fraction separation [9], chemical processing [10], and the study of emissions of granular solids—in various concentrations in mixture with air and water—from volcanoes [11]. Some of the seminal theoretical development in the field of multi-phase flow was published by Anderson and Jackson [12] for the description of domain-averaged flow of solid particle–gas systems and by Ishii, originally in 1975, and significantly updated and expanded by Ishii and Hibiki [13] for the description of gas–liquid flows.

For the purposes of the present study, the constant particle viscosity methodology as synthesized and presented by Enwald *et al.* [14] and by Johansson *et al.* [15] was modified appropriately, validated by use of experimental results reported by Anjaneyulu and Khakhar [12] then subsequently used in conjunction with soil parameters from the data assembled and presented by Cho *et al.* [16] in order to put forward a first step toward the development of a methodology for more appropriately treating the soil–air rheology that is applicable to mine blast.

DOI: 10.1002/fld

The tools developed during this study represent a step toward a better understanding and quantification of the effect of mine blast soil ejecta on ground vehicle structures and, given sufficient future refinement and validation with experimental data, their application is expected to reduce development costs and improve the robustness of mine-protected ground vehicle blast mitigation designs.

THE GAS–PARTICLE FLOW MODEL

Following the development presented in Johansson *et al.* [15], the governing continuity and momentum balance equations, developed by [13], that were used for the particle–air flow are

$$\frac{\partial}{\partial t}(\varepsilon_{\mathrm{g}}\rho_{\mathrm{g}})+\nabla\cdot(\varepsilon_{\mathrm{g}}\rho_{\mathrm{g}}U_{\mathrm{g}})=0 \tag{1}$$

$$\frac{\partial}{\partial t}(\varepsilon_{\mathrm{g}}\rho_{\mathrm{g}}U_{\mathrm{g}})+\nabla\cdot(\varepsilon_{\mathrm{g}}\rho_{\mathrm{g}}U_{\mathrm{g}}U_{\mathrm{g}})=\nabla\cdot\varepsilon_{\mathrm{g}}\tau_{\mathrm{g}}+\varepsilon_{\mathrm{g}}\rho_{\mathrm{g}}\mathbf{g}-\varepsilon_{\mathrm{g}}\nabla P-\beta(U_{\mathrm{g}}-U_{\mathrm{p}}) \tag{2}$$

for the gaseous, air, component (g), and

$$\frac{\partial}{\partial t}(\varepsilon_{\mathrm{p}}\rho_{\mathrm{p}})+\nabla\cdot(\varepsilon_{\mathrm{p}}\rho_{\mathrm{p}}U_{\mathrm{p}})=0 \tag{3}$$

$$\frac{\partial}{\partial t}(\varepsilon_{\mathrm{p}}\rho_{\mathrm{p}}U_{\mathrm{p}})+\nabla\cdot(\varepsilon_{\mathrm{p}}\rho_{\mathrm{p}}U_{\mathrm{p}}U_{\mathrm{p}})=\nabla\cdot\varepsilon_{\mathrm{p}}\tau_{\mathrm{p}}+\varepsilon_{\mathrm{p}}\rho_{\mathrm{p}}\mathbf{g}-\varepsilon_{\mathrm{p}}\nabla P-\nabla P_{\mathrm{p}}+\beta(U_{\mathrm{g}}-U_{\mathrm{p}}) \tag{4}$$

for the particulate components. ε is the volume fraction, ρ is the density, U is the velocity vector, τ is the viscous stress tensor, $\mathbf{g}$ is the gravitational acceleration vector, P is the static pressure, β is the interphase momentum transfer coefficient and P_{p} is an estimate of the particle–particle interaction force. The total volume fraction is equal to one, hence

$$\varepsilon_{\mathrm{g}}+\varepsilon_{\mathrm{p}}=1 \tag{5}$$

The viscous shear stress tensor was modeled, for each phase, by

$$\tau_l=(\xi_l-\tfrac{2}{3}\mu_l)(\nabla\cdot U_l)I+2\mu_l S_l \tag{6}$$

where ξ_l represents bulk viscosity, μ_l is the dynamic viscosity, and S_l is the rate of deformation tensor

$$S_l=\tfrac{1}{2}(\nabla U_l+(\nabla U_l)^{\mathrm{T}}) \tag{7}$$

Based on the findings of van Wachem *et al.* [17] the correlation, developed by Wen and Yu [18], for the interphase momentum transfer coefficient β that was used is

$$\beta=\frac{3}{4}C_{\mathrm{D}}\frac{(1-\varepsilon_{\mathrm{p}})\varepsilon_{\mathrm{p}}\rho_{\mathrm{g}}|U_{\mathrm{g}}-U_{\mathrm{p}}|}{\phi d_{\mathrm{p}}}(1-\varepsilon_{\mathrm{p}})^{-2.65} \tag{8}$$

where d_{p} is the mean particle diameter, φ is the particle sphericity, and C_{D} is the coefficient of drag for a single sphere.

DOI: 10.1002/fld

The correlation used for the single sphere drag coefficient C_D was presented by Rowe [19] and is

$$C_D = \frac{24}{Re_p(1-\varepsilon_p)}\{1+0.15[(1-\varepsilon_p)Re_p]^{0.687}\} \quad \text{for } (1-Re_p)<1000$$
$$C_D = 0.44 \quad \text{for } (1-Re_p)\geqslant 1000 \tag{9}$$

Re_p is the particle Reynolds number and is defined as

$$Re_p = \frac{\phi d_p \rho_g |U_g - U_p|}{\mu_g} \tag{10}$$

Finally, the scale of the particle–particle interaction force P_p was estimated by means of [20]

$$\nabla P_p = G_0 e^{-c(\varepsilon_g - \varepsilon_{g,min})} \cdot \nabla \varepsilon_p \tag{11}$$

where G_0 and c are empirically determined constants, ε_g is gas-phase volume fraction, and $\varepsilon_{g,min}$ is the smallest possible gas volume fraction. The viscosity of the particle phase was treated as a constant according to the so-called constant particle viscosity method [15].

MODEL FOR FLOW BEHAVIOR

Model geometry

The geometry used in all cases is the geometry that was employed by Anjaneyulu and Khakhar [10] in their experimental study of the rheological behavior of an air–glass bead fluidized bed (Figure 1). A rotating cylinder imparts shear stress to an annular fluidized bed containing various mixtures of air and particles and the gross particle flow behavior is measured and deduced. Boundary conditions at the cylinder walls, based on Anjaneyulu and Khakhar's conclusions for the mixture

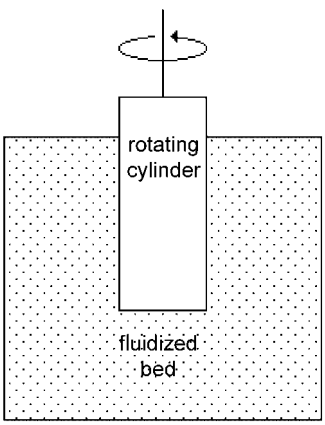

Figure 1. Simplified model geometry for analytical and numerical test cases, inner rotating cylinder radius = 0.006 m, fluidized bed outer radius = 0.0325 m.

DOI: 10.1002/fld

are assumed to be no slip. The radius of the rotating cylinder is 0.006 m, the outer radius of the bed is 0.0325 m. The cylinder rate of rotation is $\frac{5}{6}$ rev/s.

Equations of motion for test cases

It was assumed, based on the experimental results reported by Anjaneyulu and Khakhar [11], that the flow was unidirectional azimuthal (q-direction) flow. Based on the same findings it was also assumed that no-slip boundary conditions could be applied and that there were no edge effects.

The continuity relations, Equations (1) and (3), vanish and after some simplification, the fluid flow is defined using the following three relations:

$$-\rho_{\mathrm{p}}\frac{u_{\theta,\mathrm{p}}^2}{r}=-G_0\mathrm{e}^{-c(\varepsilon_{\mathrm{g}}-\varepsilon_{\mathrm{g,min}})}\cdot\frac{\partial\varepsilon_{\mathrm{p}}}{\partial r} \tag{12}$$

$$\mu_{\mathrm{g}}\left[\frac{\partial}{\partial r}\varepsilon_{\mathrm{g}}\left(\frac{1}{r}\frac{\partial}{\partial r}(ru_{\theta,\mathrm{g}})\right)\right]-\beta(u_{\theta,\mathrm{g}}-u_{\theta,\mathrm{p}})=0 \tag{13}$$

$$\mu_{\mathrm{p}}\left[\frac{\partial}{\partial r}\varepsilon_{\mathrm{p}}\left(\frac{1}{r}\frac{\partial}{\partial r}(ru_{\theta,\mathrm{p}})\right)\right]+\beta(u_{\theta,\mathrm{g}}-u_{\theta,\mathrm{p}})=0 \tag{14}$$

Definition of boundary conditions

As stated before, it was demonstrated by Anjaneyulu and Khakhar [11] that there was no slip at the walls of the internal rotating cylinder as well as at the wall of the outer cylinder.

This leads to definition of the boundary conditions for the problem, which are

$$u_{\theta,k}(r=r_{\mathrm{i}})=2\pi r_{\mathrm{i}}\Omega_0 \tag{15}$$

$$u_{\theta,k}(r=r_{\mathrm{o}})=0 \tag{16}$$

where $r_{\mathrm{i}}, r_{\mathrm{o}}$, and Ω_0 are rotating cylinder radius, outer wall radius, and rotational speed of inner cylinder, respectively.

Physical properties for gas and particle phases

The experimental data from Anjaneyulu and Khakhar [10] used in this work were those generated under minimum fluidization conditions, viz, under those conditions for which the pressure drop through the column matched the body force, from gravity, that was exerted on the material contained in the column.

The choice for the value of ε_{p} was based on results reported in the literature for minimum fluidization conditions. Olowson and Almstedt [21] suggest that, for minimum fluidization, the particle volume fraction ε_{p} is 0.54. McCabe *et al.* [22], suggest that, for nearly spherical particles, ε_{p} should be approximately 0.55–0.60, decreasing a bit with increasing particle size.

Based on the experimental conditions and the geometry, a scale analysis was performed on Equation (12). Order of magnitude estimates of the various quantities in Equation (12) is presented in Table I.

Based on these estimates, it was determined that the radial variation of the particle volume fraction $\Delta\varepsilon_{\mathrm{p}}$ across the bed was of the order of 10^{-3}, whereas the order of magnitude of ε_{p} was

DOI: 10.1002/fld

Table I. Parameter orders of magnitude for the estimate of radial variation of particle volume fraction ε_p.

Parameter	Scale	Units
ρ	1.00E+03	kg/m^3
u^2	1.00E−04	$(m/s)^2$
R	1.00E−02	m
$G_0 \exp[-c(\varepsilon_{p,max} - \varepsilon_p)]$	1.00E+02	N/m^2
Δr	1.00E−02	m
ε_p and $\varepsilon_{p,max}$	1.00E−01	dimensionless

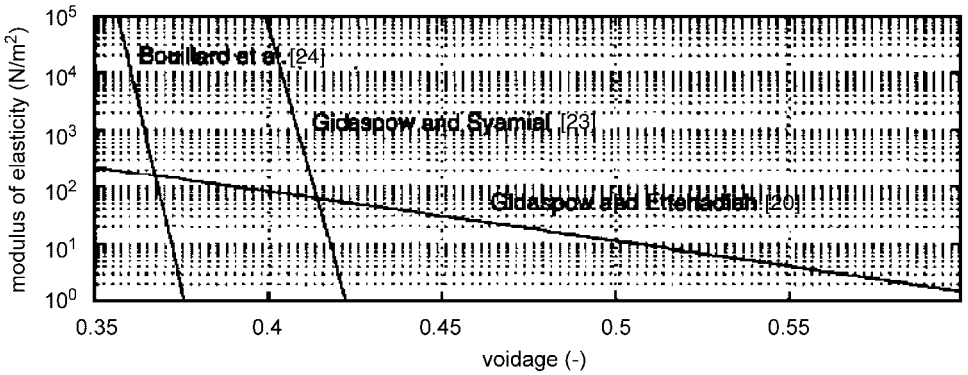

Figure 2. Correlations for $G_0 \exp[-c(\varepsilon_{p,max} - \varepsilon_p)]$. Note that voidage is the gas-phase gas fraction ε_g and is equal to $1 - \varepsilon_p$ [15].

Table II. Physical properties of glass beads and air.

Property	Air (20°C)	Glass beads	Units
Sphericity ϕ	—	1.00E+00	dimensionless
Mean particle diameter d_p	—	9.00E−04	m
Viscosity μ	1.20E+00	—	Pa s
Density ρ	1.88E−05	2.50E+03	kg/m^3
Volume fraction ε	4.60E−01	5.40E−01	dimensionless

10^{-1}. The scale of $G_0 \exp[-c(\varepsilon_{p,max} - \varepsilon_p)]$ was based on the results of Gidaspow and Ettehadieh [20] as presented in Enwald *et al.* [15] (Figure 2). The results from Gidaspow and Ettehadieh [20] were chosen rather than those from Gidaspow and Syamlal [23] or Bouillard *et al.* [24] since only the results reported in Gidaspow and Ettehadieh [20] contained the volume fractions assumed for the current problem.

Values for other physical properties associated with the flow problem test case are contained in Table II.

DOI: 10.1002/fld

Discretization of equations of motion

Given the determination, via scale analysis, that ε_p was relatively constant across the radial position of the bed, expansion and rearrangement of Equations (13) and (14) yields the two relations that were used for the discretization.

$$\frac{\partial^2 u_{\theta,g}}{\partial r^2}+\frac{1}{r}\frac{\partial u_{\theta,g}}{\partial r}-\left(\frac{1}{r^2}+\frac{\beta}{\varepsilon_g\mu_g}\right)u_{\theta,g}+\frac{\beta}{\varepsilon_g\mu_g}u_{\theta,p}=0 \tag{17}$$

$$\frac{\partial^2 u_{\theta,p}}{\partial r^2}+\frac{1}{r}\frac{\partial u_{\theta,p}}{\partial r}-\left(\frac{1}{r^2}+\frac{\beta}{\varepsilon_p\mu_p}\right)u_{\theta,p}+\frac{\beta}{\varepsilon_p\mu_p}u_{\theta,g}=0 \tag{18}$$

First and second derivatives were approximated using central differences in order to limit the truncation error to be of the order of $(\Delta r)^2$.

$$\frac{\partial^2 u_{\theta,g}}{\partial r^2}=\frac{u_{\theta,g,j+1}-2u_{\theta,g,j}+u_{\theta,g,j-1}}{(\Delta r)^2}+O[(\Delta r)^2] \tag{19}$$

$$\frac{\partial^2 u_{\theta,p}}{\partial r^2}=\frac{u_{\theta,p,j+1}-2u_{\theta,p,j}+u_{\theta,p,j-1}}{(\Delta r)^2}+O[(\Delta r)^2] \tag{20}$$

$$\frac{\partial u_{\theta,g}}{\partial r}=\frac{u_{\theta,g,j+1}-u_{\theta,g,j-1}}{2(\Delta r)}+O[(\Delta r)^2] \tag{21}$$

$$\frac{\partial u_{\theta,p}}{\partial r}=\frac{u_{\theta,p,j+1}-u_{\theta,p,j-1}}{2(\Delta r)}+O[(\Delta r)^2] \tag{22}$$

Substitution of these expressions for the derivatives into Equations (17) and (18) led, after some rearrangement, to the discretized equations that were implemented in the code

$$u_{\theta,g,j}=K_1u_{\theta,g,j+1}+K_2u_{\theta,g,j-1}+K_3u_{\theta,p,j} \tag{23}$$

$$u_{\theta,p,j}=K_1u_{\theta,p,j+1}+K_2u_{\theta,p,j-1}+K_3u_{\theta,g,j} \tag{24}$$

where K_1-K_6 are coefficients that are combinations of the various parameters in Equations (17)–(22) and that, it must be noted, depend on the values of the radial position as well as of the particle and air velocities.

Solution method

The Gauss–Seidel iteration method was used for the numerical solution of the flow equations, but with the boundary conditions for the particle and gas velocities at r_i and r_o enforced by constraint of the velocity values to constant values at these radial locations.

Solution method check: comparison of numerical results with analytical results for single component Newtonian flow problem

The accuracy of the flow problem solution method was investigated by comparing numerical results from the code with the analytical solution for the single component, Newtonian viscosity problem.

DOI: 10.1002/fld

The problem statement, for this case, is

$$\mu\left[\frac{\partial}{\partial r}\left(\frac{1}{r}\frac{\partial}{\partial r}(ru_\theta)\right)\right]=0 \tag{25}$$

$$u_\theta(r=r_\mathrm{i})=2\pi r_\mathrm{i}\Omega_0 \tag{26}$$

$$u_\theta(r=r_\mathrm{o})=0 \tag{27}$$

with analytical solution given by

$$u_\theta(r)=\frac{\Omega_0\kappa r_\mathrm{o}}{\left(\kappa-\frac{1}{\kappa}\right)}\left(\frac{r}{r_\mathrm{o}}-\frac{r_\mathrm{o}}{r}\right) \tag{28}$$

where

$$\kappa=\frac{r_\mathrm{i}}{r_\mathrm{o}} \tag{29}$$

The analytical and numerical solutions to this problem are compared in Figure 3. It can be seen that the numerical results very closely matched the analytical solution. It is noteworthy that the radial velocity distribution is determined only by radial position, inner radius value, outer radius value, and angular velocity of inner cylinder and that flow behavior is not dependent on fluid intrinsic properties such as viscosity or density.

Parameter identification: air velocity distribution for two component flow

As a result of the nature of the algorithm used to solve Equations (23) and (24), it was found that the solutions for both the air and particle phases converged identically—independent of the

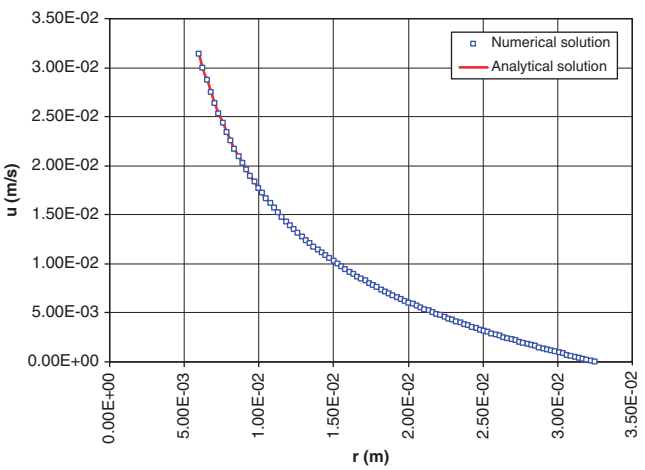

Figure 3. Comparison of numerical and analytical solution to the single component Newtonian flow problem.

DOI: 10.1002/fld

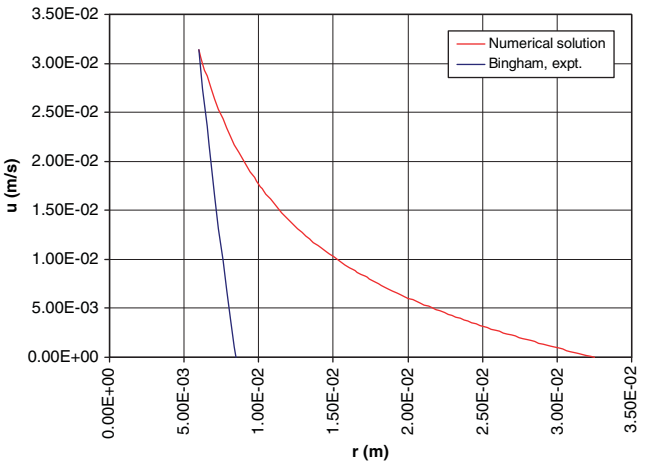

Figure 4. Comparison of experimental results with initial numerical solution derived with air velocity calculated by Equation (23).

input values for air or particle viscosities, for particle sphericity, for particle diameter, and for air density—to the analytical solution represented by Equation (28) and shown in Figure 3. This was found to be a result, during solution convergence, of the tendency of the air and particle velocities to converge toward one another. This caused the scaling of the coupling coefficients β_i to grow large and forced the velocity distributions for the two components to completely converge to one another. This result did not match the Bingham plastic experimental results as modeled and reported by Anjaneyulu and Khakhar [10] (cf. Figure 4).

In an effort to better determine the velocity distributions without completely revamping the solution algorithm, the values for the air velocity were constrained to be the multiples of the velocities of the solid fraction, viz,

$$u_{\theta,g,i} = K u_{\theta,p,i} \tag{30}$$

where K is a constant. The results for $K>1$, i.e. for air velocity>particle velocity did not, in general, converge to yield any physically plausible results. Neither did the solutions for $K=1$.

Some results for various values of $K<1$ are shown in Figures 5 and 6 for particle viscosity values set to 1.0 and 0.01 Pa s. For the case of particle viscosity set to 1.0 Pa s (Figure 5), it can be seen that, as K decreases from 0.9 to 0.0, there is a moderate movement toward the experimental results. For the case of particle viscosity set to 0.01 Pa s (Figure 6), it can be seen that as K decreases toward a value of 0.0, the particle velocity distribution seems to fairly closely converge to the experimental result.

Although, the results appeared to converge toward the experimental result, more work needs to be done in order to be sure that the particle velocity distributions approach each other as a result of the physics rather than simply as a result of the mathematical behavior of the current model. It is not, at this point, clear that the azimuthal air velocity, in this physical situation, would necessarily tend toward 0 or even that it would necessarily be lower than the particle velocity. To this end,

DOI: 10.1002/fld

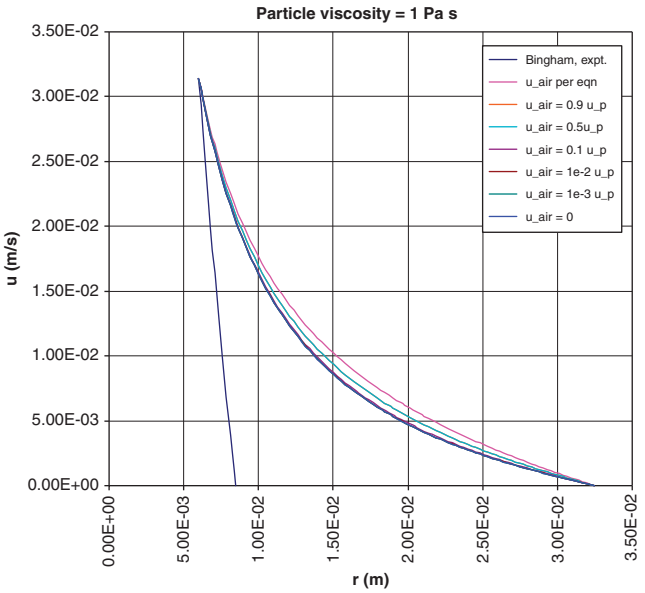

Figure 5. Effect of decreasing the air-phase velocity for the case of particle viscosity = 1.0 Pa s.

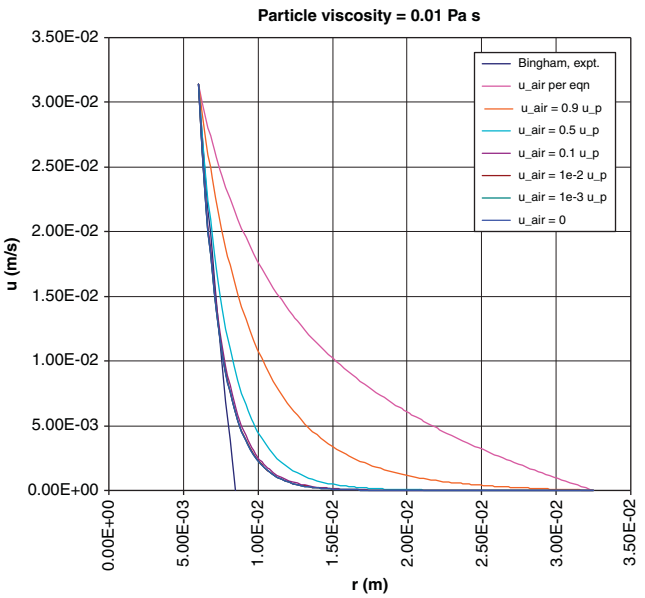

Figure 6. Effect of decreasing the air-phase velocity for the case of particle viscosity = 0.01 Pa s. The particle velocity distribution appears to approach the experimentally determined velocity distribution.

DOI: 10.1002/fld

future investigation will be conducted and will involve the numerical solution of Equations (17) and (18) using other discretization schemes. For now, however, the behavior of the model will be investigated with K, and thus the azimuthal air velocity set to 0.0.

Parameter identification: particle viscosity

A statistical technique was employed to determine the value for the particle viscosity that would enable the numerical solution to most closely match, using the measure of mean-square difference from the experimental results.

Mean-square error (MSE) was calculated as

$$\mathrm{MSE} = \frac{\sum_{j=1}^{m} (u_{\mathrm{experimental},j} - u_{\mathrm{numerical},j})^2}{m} \tag{31}$$

where u_j are the experimentally reported and numerically calculated values of the particle velocity, j is as used in the discretization, and $j = m$ is the index of the value of the radial position for which the value of the experimentally reported particle velocity is less than about 10% of its maximum value. The level of particle viscosity that allowed the numerical solution to most closely approach the experimentally determined solution was 0.0095 Pa s (Figure 7).

Effect of grid spacing on solution

A comparison of solutions generated by means of different grid spacing is presented in Figure 8, for solutions involving 25, 50, and 100 grid points. It can be seen that similar convergence was achieved for all three levels of spacing between grid points and that all three regimes seemed to approach the experimental result in a similar fashion.

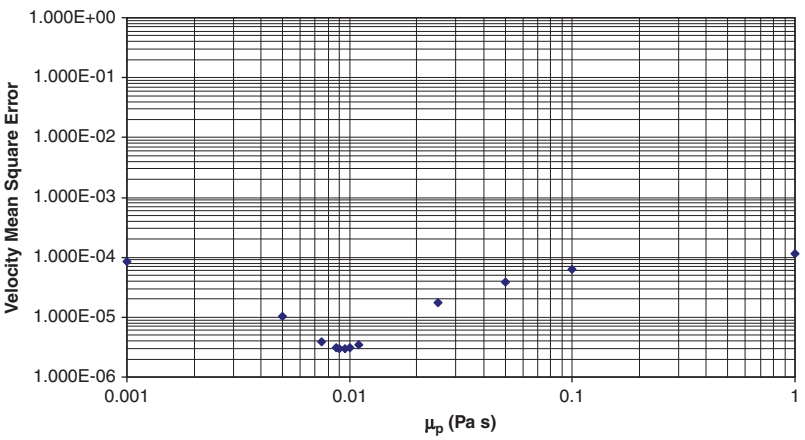

Figure 7. Material identification for the best value of particle viscosity based on mean-square error between experiment and model. Best value of particle viscosity appeared to be 0.0095 Pa s.

DOI: 10.1002/fld

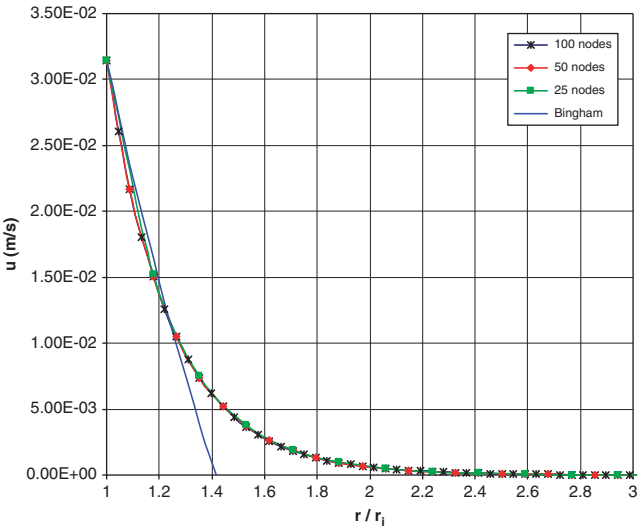

Figure 8. Comparison of numerical results for various mesh sizes versus experimental (Bingham plastic) results.

Iteration convergence

The convergence of the iterated solution was measured by means of the root mean-square error (RMSE) between iterations according to

$$\mathrm{RMSE}=\sqrt{\frac{\sum_{j=1}^{n-1}(u_k-u_{k-1})^2}{n-1}} \tag{32}$$

where k refers to the kth iteration, j corresponds to the radial position r_i, and n corresponds to the maximum value of j, viz, the maximum radius is denoted, within the FORTRAN code as r_n. The iteration results are shown in Figure 9, where it can be seen that, for the case of 100 grid points and particle viscosity 0.0095 Pa s, excellent convergence appears to have occurred after about 400 iterations, i.e. at that point RMSE$<$1%.

Summary of experimental results

The results that were reported by Anjaneyulu and Khakhar [10] were given in terms of the Bingham plastic parameters as

$$\begin{aligned}\tau_{r\theta} &= \tau_y+\mu\dot{\gamma}, \quad \tau_{r\theta}>\tau_y\\ \tau_{r\theta} &= \tau_y, \quad \tau_{r\theta}\leqslant\tau_y\end{aligned} \tag{33}$$

where $\dot{\gamma}$ is the rate of deformation, $\tau_{r\theta}$ is the shear stress, μ is the viscosity, and τ_y is the yield stress, viz, the level of shear stress below which no deformation will occur. The data are summarized in Table III. $r_\mathrm{interface}$ is defined as the value of the radius for which the shear stress falls to the level of τ_y at which point the fluid begins to behave as a solid. Anjaneyulu and Khakhar [10] estimated the

DOI: 10.1002/fld

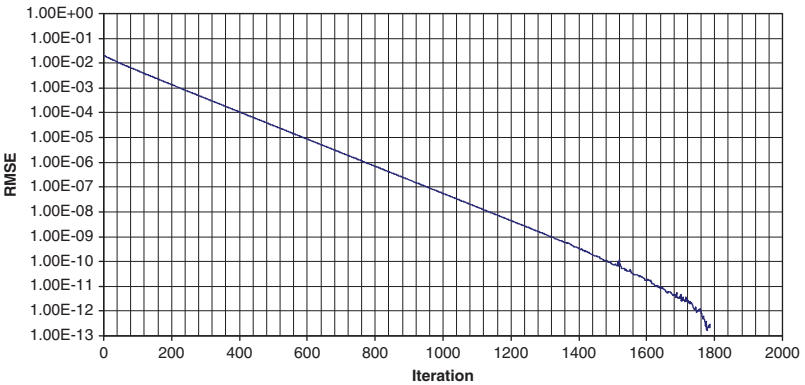

Figure 9. Convergence of iterations for the case of particle viscosity 0.0095 Pa s and 100 grid points.

Table III. Summary of Anjaneyulu and Khakhar [10] experimental data.

Particle diameter	9.00E−04	m
Inner cylinder radius	6.00E−03	m
Yield stress	4.50E+00	Pa
Viscosity	2.00E−01	Pa s
Shear stress at inner wall	9.00E+00	Pa s
Rotational speed	8.33E−01	rev/s
Theoretical $r_{\text{interface}}/r_{\text{i}}$	1.41E+00	
Actual $r_{\text{interface}}/r_{\text{i}}$	2.2E+00	

Bingham plastic parameters using least-squares techniques and noted that a significant difference was measured between the theoretical (Bingham model) and directly observed ratio of critical radius to inner cylinder radius, viz, the theoretical ratio was 1.41 whereas the ratio that was actually observed was 2.2.

The computational model seemed to show results for this apparent disparity in critical radius that fit the experimental data better than did the Bingham model as evidenced by the intersection point of the two-phase CFD velocity result with the r/r_{i} axis at a value of 2.7 (Figure 10).

Flow effects resulting from variation of sphericity and particle diameter

Comparisons, using the numerical model developed for this work, of flow behavior resulting from the variation of sphericity and particle size were performed based on particle properties reported by Cho *et al.* [16]. Sphericity is defined as the diameter of the largest sphere that can be inscribed on a particle relative to the diameter of the smallest sphere that can be circumscribed on a particle.

The results of these calculations are shown in Figures 11 and 12. The calculations seemed to show that resistance to flow increased with decreasing particle size and that resistance to flow increased with decreasing sphericity. Figure 13, which, shows results for several real materials, also appears to exhibit the same trend of increasing flow resistance with decreasing particle size and sphericity. The reason for this can be deduced based on inspection of Equations (8)–(10). As either sphericity or particle size decreases, the particle Reynolds number, coefficient of drag, and

DOI: 10.1002/fld

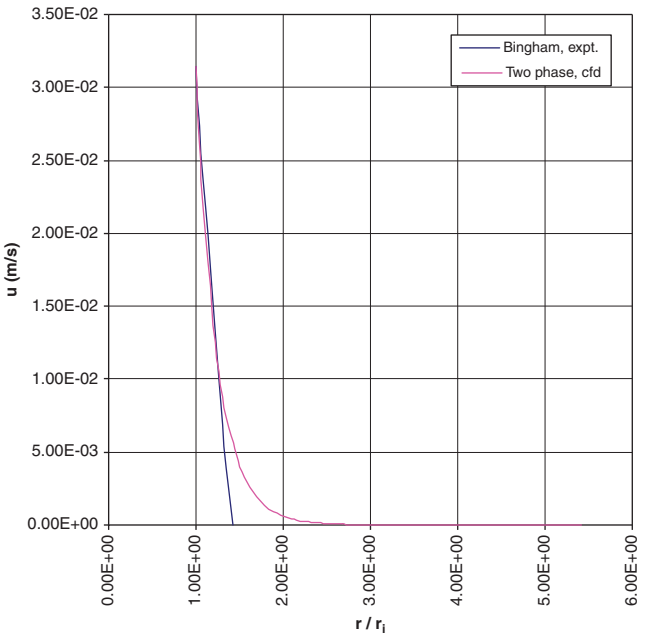

Figure 10. Comparison of experimental and numerical velocity distributions as a function of r/r_{i}. Note that the intersection of the CFD result with the r/r_{i} axis seemed to match the experimental results in Table III better than the Bingham fluid model.

coupling factor will increase, thereby increasing the resistance to flow. It should not be tacitly concluded that this trend is correct simply based on the correlations. Future work will involve more extensive comparison of these results with relevant experimental results, if they are available, in order to more fully verify whether the current model adequately predicts two-phase fluid flow behavior.

Extensive searches for relevant comparison data have, to date, not been successful. If adequate data cannot be found, a different physical regime, for which more extensive validation data can be identified, will be modeled using the techniques developed for this work. It is not inconceivable that the effects of sphericity and average particle diameter might depend on the geometry and other characteristics of the flow regime and particle and fluid components.

SUMMARY AND CONCLUSIONS

It was determined that the two-phase fluid model developed for this work seemed to match the data from Anjaneyulu and Khakhar [10] fairly well. Although it was a somewhat simple model, it appeared to yield fairly accurate results. Before a tacit assumption is made; however, that this model accurately predicts more general two-phase flow phenomena, it needs to be more fully validated.

It cannot be assumed that it is physically correct to assume that the azimuthal velocity tends toward 0 or that it is even, in general, lower than the apparent particle velocity. The model will

DOI: 10.1002/fld

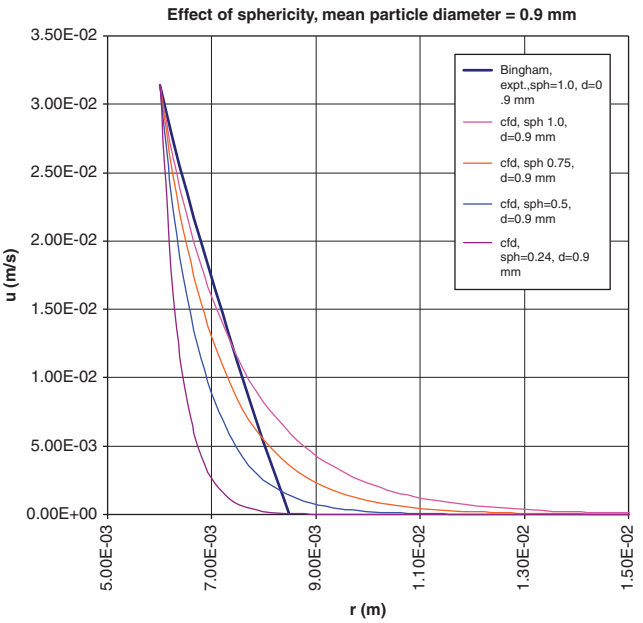

Figure 11. Effect of sphericity on velocity distribution and resistance to flow. As sphericity decreased, the calculated resistance to the flow increased.

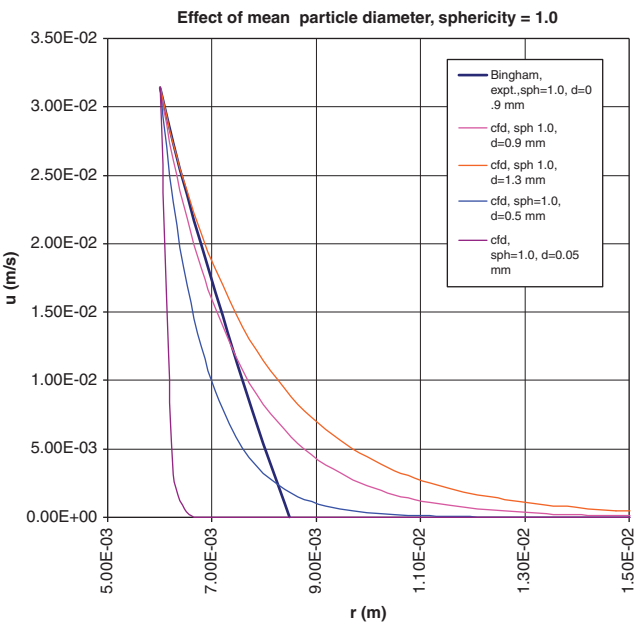

Figure 12. Effect of average particle diameter on velocity distribution and resistance to flow. As particle diameter decreased, calculated resistance to the flow increased.

DOI: 10.1002/fld

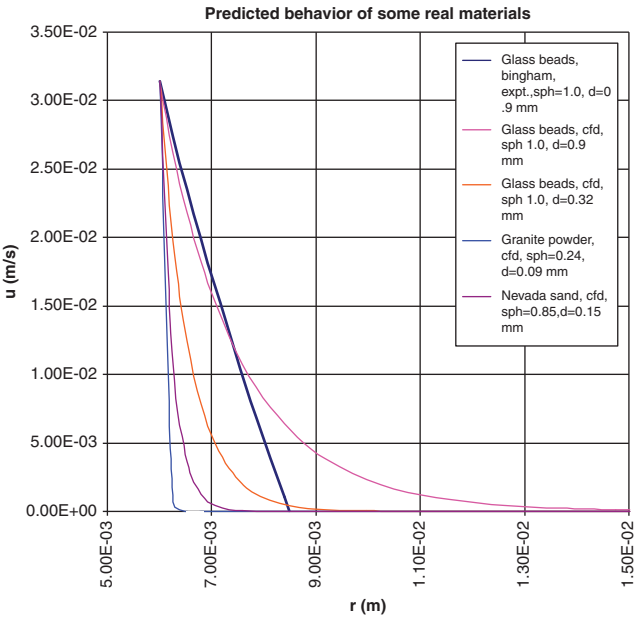

Figure 13. Effect of sphericity and average particle diameter, for several real materials, on velocity distribution and resistance to flow. As these parameters decreased, calculated resistance to the flow increased.

be discretized using a different scheme, and Equations (17) and (18) will be solved numerically using the new scheme in order to examine this issue more carefully.

Future efforts relative to the effects of adding radial, z-direction, and turbulent effects will be investigated by means of problems involving more complex geometry in order to better validate this model for blast applications.

Finally, it must be noted that the work presented in this paper was for a low Mach number, steady-state problem, whereas mine blast problems most often involve the detonation of high explosives with attendant movement of shock discontinuities, fluid, and solid particles at relatively high velocities. If this methodology is to prove useful when applied to actual mine blast problems then it must also be adapted and validated for transient problems using initial and boundary conditions that will create the appropriate shock phenomena.

REFERENCES

1. Williams K, McLennan S. A numerical analysis of mine blast effects on simplified target geometries. *DRDC—Valcartier Technical Memorandum No. 2002-260*, Defence R&D Canada-Valcartier, 2003.
2. Neuberger A, Peles S, Rittel D. Scaling the response of circular plates subjected to large and close-range spherical explosions. Part I: air-blast loading. *International Journal of Impact Engineering* 2007; **34**:859–873.
3. Drucker DC, Prager W. Soil mechanics and plastic analysis on limit design. *Quarterly of Applied Mathematics* 1952; **10**:157–165.
4. Neuberger A, Peles S, Rittel D. Scaling the response of circular plates subjected to large and close-range spherical explosions. Part II: buried charges. *International Journal of Impact Engineering* 2007; **34**:874–882.
5. Tong X, Tuan CY. Viscoplastic cap model for soils under high strain rate loading. *Journal of Geotechnical and Geo-Environmental Engineering* 2007; **133**(2):206–214.

DOI: 10.1002/fld

6. Laine L, Ranestad O, Sandvik A, Snekkevik A. Numerical simulation of anti-tank mine detonations. *Proceedings of the 12th Conference of the American Physical Society*, *Topical Group on Shock Compression of Condensed Matter*, vol. 620. American Physical Society: Atlanta, U.S.A., 2001; 431–434.
7. Bergeron D, Walker R, Coffey C. Detonation of 100-gram anti-personnel mine surrogate charges in sand: a test case for computer code validation. *SUFFIELD REPORT No. 668. DRES-SR-668*, Defence Research Establishment Suffield, 1998.
8. Hlady SL. Effect of soil parameters on landmine blast. *Eighteenth International Symposium on the Military Aspects of Blast and Shock*, Bad Reichenhall, Germany, 2004.
9. Zhao Y, Wei L. Rheology of gas–solid fluidized bed. *Fuel Processing Technology* 2000; **68**(2):153–160.
10. Anjaneyulu TB, Khakhar DV. Rheology of a gas-fluidized bed. *Powder Technology* 1995; **83**(1):29–34.
11. Dartevelle S. Numerical modeling of geophysical granular flows: 1. A comprehensive approach to granular rheologies and geophysical multiphase flows. *Geochemistry*, *Geophysics*, *Geosystems* 2004; **5**:1–28.
12. Anderson TB, Jackson R. A fluid mechanical description of fluidized beds. *Industrial and Engineering Chemistry Fundamentals* 1967; **6**:527–539.
13. Ishii M, Hibiki T. *Thermo-Fluid Dynamics of Two-Phase Flow*. Springer: New York, 2006.
14. Enwald H, Peirano E, Almstedt AE. Eulerian two-phase flow theory applied to fluidization. *International Journal of Multiphase Flow* 1996; **22**(Suppl.):21–66.
15. Johansson K, van Wachem BGM, Almstedt AE. Experimental validation of CFD models for fluidized beds: influence of particle stress models, gas phase compressibility and air inflow models. *Chemical Engineering Science* 2006; **61**:1705–1717.
16. Cho GC, Dodds J, Santamarina JC. Shape effects on packing density, stiffness, and strength: natural and crushed sands. *Journal of Geotechnical and Geo-Environmental Engineering* 2006; **132**(5):591–602.
17. van Wachem BGM, Schouten JC, van den Bleek CM, van Sinclair JL. Comparative analysis of CFD models of dense gas–solid systems. *AIChE Journal* 2001; **47**:1035–1051.
18. Wen CY, Yu YH. *Mechanics of Fluidization*. Chemical Engineering Progress Symposium Series, vol. 62. Wiley Interscience: 2001; 100–111.
19. Rowe PN. Drag forces in a hydraulic model of a fluidized bed, part II. *Transactions of the Institution of Chemical Engineers* 1961; **32**:175–180.
20. Gidaspow D, Ettehadieh B. Fluidization in two-dimensional beds with a jet III hydrodynamic modelling. *Industrial and Engineering Chemistry Fundamentals* 1983; **22**:193–201.
21. Olowson PA, Almstedt AE. Influence of pressure on the minimum fluidization velocity. *Chemical Engineering Science* 1991; **46**:637–640.
22. McCabe WE, Smith JC, Harriott P. *Unit Operations of Chemical Engineering*. McGraw-Hill: New York, 2001.
23. Gidaspow D, Syamlal M. Solid–gas critical flow. *AIChE Meeting*, Chicago, 10–15 November 1985.
24. Bouillard JX, Lyczkowski RW, Gidaspow D. Porosity distributions in a fluidized bed with an immersed obstacle. *AIChE Journal* 1989; **35**:908–922.

DOI: 10.1002/fld